ACS Energy LETTERS

http://pubs.acs.org/journal/aelccp

Silica-Encapsulated Perovskite Nanocrystals for X-ray-Activated Singlet Oxygen Production and Radiotherapy Application

Francesco Carulli,*[,†] Mengda He,[†] Francesca Cova,[†] Andrea Erroi, Liang Li,* and Sergio Brovelli*

Cite This: *ACS Energy Lett.* 2023, 8, 1795−1802

Read Online

ACCESS | Metrics & More | Article Recommendations | Supporting Information

ABSTRACT: Multicomponent systems consisting of lead halide perovskite nanocrystals ($CsPbX_3$-NCs, X = Br, I) grown inside mesoporous silica nanospheres (NSs) with selectively sealed pores combine intense scintillation and strong interaction with ionizing radiation of $CsPbX_3$ NCs with the chemical robustness in aqueous environment of silica particles, offering potentially promising candidates for enhanced radiotherapy and radio-imaging strategies. We demonstrate that $CsPbX_3$ NCs boost the generation of singlet oxygen species ($^1O_2$) in water under X-ray irradiation and that the encapsulation into sealed SiO_2 NSs guarantees perfect preservation of the inner NCs after prolonged storage in harsh conditions. We find that the $^1O_2$ production is triggered by the electromagnetic shower released by the $CsPbX_3$ NCs with a striking correlation with the halide composition (I_3 > $I_{3-x}Br_x$ > Br_3). This opens the possibility of designing multifunctional radio-sensitizers able to reduce the local delivered dose and the undesired collateral effects in the surrounding healthy tissues by improving a localized cytotoxic effect of therapeutic treatments and concomitantly enabling optical diagnostics by radio imaging.

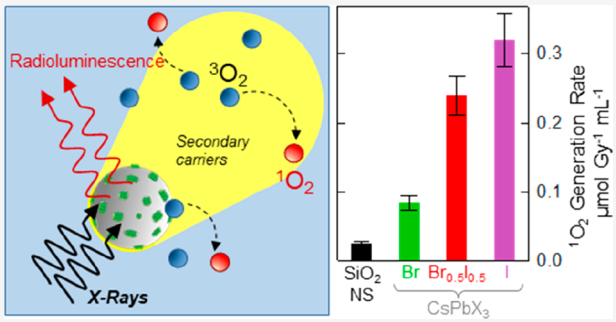

In the last decades, interest in nanoparticles in the biomedical field experienced a rapid growth due to the tunability of their physical and chemical properties and their rich surface chemistry that enables specific functionalization by design.[1,2] Different classes of functional nanoparticles, including metals, semiconductors,[3,4] metal/lanthanide oxides,[5,6] and organic or hybrid systems,[7,8] have found successful application in several medical branches, such as nanotherapy, diagnostics, and imaging.[9−11] Today, one of the most advanced biomedical uses of nanoparticles is offered by their strong interaction with ionizing radiation, which makes it possible to improve the effectiveness of conventional cancer treatments[12] and imaging techniques.[13] In oncological therapies, one of the most adopted medical treatments is radiotherapy (RT, ca. 50% of total cases),[14,15] a noninvasive technique typically consisting of the local release of the energy of X-rays via photoelectric effect and/or Compton scattering to stop tumor cell proliferation, either directly by damaging their DNA or indirectly by forming cytotoxic free radicals—such as singlet oxygen ($^1O_2$), superoxide (O^{2-}) or hydrogen peroxide (H_2O_2)—commonly termed reactive oxygen species (ROS), upon interaction with the cellular aqueous environment.[16] Currently, in order to achieve significant therapeutic effects, patients are exposed to high doses of X-ray radiation (typically 40−60 Gy in a complete RT treatment) that carry a high risk of damaging surrounding healthy areas, due to the difficulty of finely focusing the radiotherapy exclusively on the region of interest.[17] In order to reduce X-ray exposure, several strategies have been proposed to increase the local ROS production, such as radio-stimulated photodynamic therapy and radiation catalysis.[2,18] The first is based on activating a photosensitizer responsible for the energy transfer to O_2 molecules promoting ROS production, whereas the second takes advantage of the chemical and catalytic activities of nanoparticle surfaces to enhance the generation of radiation-induced radicals by, for example, water radiolysis.[19]

Metal halide nanocrystals (NCs),[20−25] both in their most common lead-based inorganic or hybrid perovskite form ($APbX_3$, with A = Cs, methylammonium, formamidinium, X = Cl, Br, I)[26−28] or in lead-free alternatives,[29−31] have recently attracted substantial attention for ionizing radiation detec-

Received: January 31, 2023
Accepted: March 13, 2023
Published: March 17, 2023

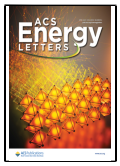

https://doi.org/10.1021/acsenergylett.3c00234
ACS Energy Lett. 2023, 8, 1795−1802

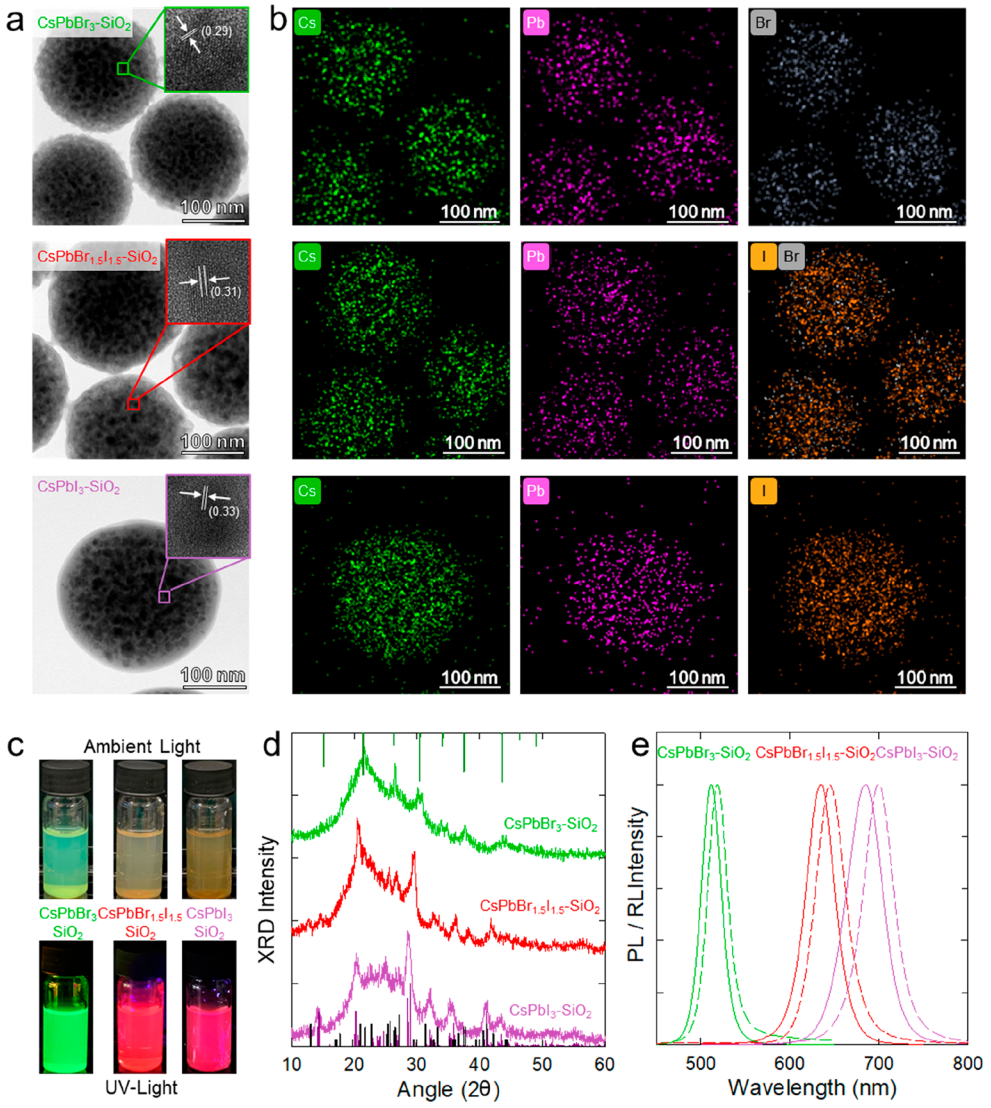

Figure 1. (a) TEM images of $CsPbBr_3$−SiO_2, $CsPbBr_{1.5}I_{1.5}$−SiO_2, and $CsPbI_3$−SiO_2 NSs. (b) HAADF-STEM images and elemental mappings on the same samples highlighting the presence of Cs (green), Pb (purple), Br (gray), and I (yellow) inside the NSs. (c) Photographs of $CsPbBr_3$−SiO_2, $CsPbBr_{1.5}I_{1.5}$−SiO_2, and $CsPbI_3$−SiO_2 in aqueous solution taken under ambient illumination (top pictures) and under UV illumination (bottom pictures). (d) XRD patterns of $CsPbBr_3$−SiO_2 (green line), $CsPbBr_{1.5}I_{1.5}$−SiO_2 (red line), and $CsPbI_3$−SiO_2 (purple line). The diffraction patterns of cubic $CsPbBr_3$ (ICSD 97852, green), orthorhombic γ-phase (ICSD 434338, violet line), and orthorhombic δ-phase (ICSD 250744, black line) of $CsPbI_3$ are also reported as references. (e) Normalized PL (solid lines) and RL (dashed lines) spectra of the same samples in dry powder form (excitation wavelength, 405 nm for PL; X-ray irradiation at 20 kV for RL).

tion,[32] prized for their high average atomic number (Z) that enhances the interaction probability with ionizing radiation ($P_i \sim Z^n$, with n = 1−5 depending on the type of radiation and interaction),[33] efficient scintillation,[34−36] and strong robustness to prolonged exposure to ionizing radiation.[35] Importantly, the easy tuning of their emission spectrum from UV to NIR further makes them interesting candidates as biological markers for radio-imaging, naturally overcoming the limitations of common fluorophores to fit the near-infrared transparency window of biological tissues.[37,38] This opens up perspectives for the simultaneous application of LHP NCs in diagnostics and therapeutics, acting as X-ray biological markers to identify and target diseased areas and simultaneously as sensitizers for enhanced radiotherapy.[39]

Despite such promise, very few examples of medical diagnostic and therapeutic strategies based on metal halide NCs have been proposed,[40−42] mostly because of their low stability in aqueous environment[43] resulting in their rapid dissolution and further consequent release of potentially harmful Pb^{2+} ions. Recently, innovative strategies for the realization of high-quality $CsPbX_3$ NCs inside impermeable host matrixes have been proposed,[44−53] including mesoporous SiO_2 particles,[54−61] semiconducting shells,[62,63] metal−organic frameworks,[64] glasses and metal oxides,[65−71] which preserve the luminescence properties of the host NCs even in harsh environments and prevent Pb dispersion in the surroundings,[29,72,73] effectively removing the constraints for the application of this class of materials in biological environments. To date, however, no study has approached the use of metal halide NCs for radiotherapy.

In this work, we aim to contribute to this endeavor by demonstrating that $CsPbX_3$ (X = Br, I) NCs directly synthesized inside mesoporous silica nanospheres (SiO_2−NSs) behave as effective X-ray sensitizers for the generation of

https://doi.org/10.1021/acsenergylett.3c00234
ACS Energy Lett. 2023, 8, 1795−1802

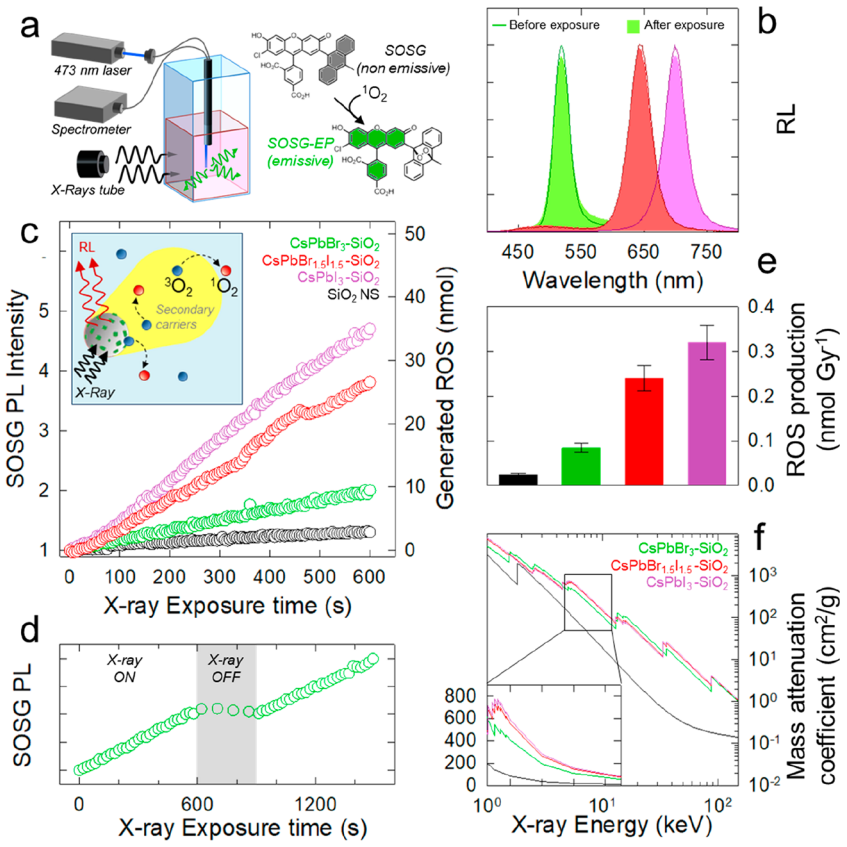

Figure 2. (a) Sketch of the experimental setup for the measurement of $^1O_2$ production under X-ray irradiation. (b) RL spectra of $CsPbBr_3$−SiO_2, $CsPbBr_{1.5}I_{1.5}$−SiO_2, and $CsPbI_3$−SiO_2 NSs before (lines) and after (shaded areas) exposure to 20 Gy dose of X-rays. The same color code is applied to all panels. (c) SOSG PL intensity (excited at 473 nm) normalized for the initial value for pristine SiO_2 NS (black circles), $CsPbBr_3$−SiO_2 (green circles), $CsPbBr_{1.5}I_{1.5}$−SiO_2 (red circles), and $CsPbI_3$−SiO_2 (purple circles) as a function of X-ray exposure time. Inset: Sketch of ROS production mechanism. (d) SOSG PL intensity excited at 473 nm during the full X-ray irradiation sequence in the presence (X-ray ON) and in the absence of simultaneous X-ray irradiation (X-ray OFF) for a solution containing $CsPBI_3$−SiO_2 NSs. (e) $^1O_2$ production rate calculated from the linear fitting of the data in panel c. (f) X-ray mass attenuation coefficient of the investigated material systems based on the NIST database.[76] In the inset the enlargement of the mass attenuation coefficient in linear scale in the energy range of the X-rays used in our experiments is reported.

$^1O_2$ species, boosting the effect of bare SiO_2 NSs by over 10-fold. Interestingly, we found that the $^1O_2$ sensitization effect is largely due to the release of secondary electrons by the $CsPbX_3$−SiO_2 NSs without quenching their radioluminescence (RL) and that neither the RL nor the photoluminescence (PL) are affected by high radiation doses or by prolonged storage in an aqueous environment (even in highly acid solutions). These results, combined with the inhibition of Pb^{2+} cation leakage outside the NS, made possible by the perfect sealing of the pores, open up the future possibility of implementing $CsPbX_3$−SiO_2 NSs as radio-stimulated markers and therapeutic agents.

$CsPbX_3$−SiO_2 NSs of different halide composition (namely, $CsPbBr_3$, $CsPbBr_{1.5}I_{1.5}$, and $CsPbI_3$) were synthesized using SiO_2 NS as templates by a solid-state confined growth technique in the presence of potassium salt as sintering agent, which promotes complete collapse of the porous structure, isolating the inner $CsPbX_3$ NCs from the outer environment and maintaining good solubility of the NSs in water. Specifically, spherical SiO_2 NSs with diameter ∼200 nm and even distribution of internal pore dimensions were dispersed in a distilled water solution containing a proper proportion of the NC precursors (see Methods in the Supporting Information for details) and kept under stirring to favor the soaking of ions inside the pores. $CsPbX_3$ NCs were subsequently synthesized inside the pores by drying at 80 °C to remove excess solvent followed by heating at 600 °C in the presence of potassium salt (K_2CO_3 and KI, respectively) to trigger the calcination reaction (details of the effects of the calcination temperature and conditions are reported in ref 54). Besides prompting the formation of $CsPbX_3$ NCs, the high temperature also favors the full collapse of the SiO_2 pores, which encloses the NCs inside the NSs and protects them from oxidation and ripening fusion. After cooling to room temperature, the $CsPbX_3$−SiO_2 NSs were washed with ultrapure water several times to remove unreacted precursors and possible products formed outside the NSs, collected via centrifugation, dried at 60 °C, and finally redispersed in water for further studies.

Transmission electron microscopy (TEM) images of $CsPbX_3$−SiO_2 NSs are reported in Figure 1a and show spherical nanoparticles comparable to the original template NSs (see Figure S1) with a slight reduction in size due to pore collapse and subsequent shrinkage during calcination (see Figure S2), without any aggregation due to interparticle cross-linking. High-angle annular dark-field scanning transmission electron microscopy (HAADF-STEM) images and the corresponding elemental mappings (Figure 1b) of $CsPbBr_3$,

https://doi.org/10.1021/acsenergylett.3c00234
ACS Energy Lett. 2023, 8, 1795−1802

$CsPbBr_{1.5}I_{1.5}$, and $CsPbI_3$ show that all constituent elements (Cs, Pb, Br, and I) are detected only at the NS structure, indicating that no NC remained outside the particles. Also importantly, the adopted calcination procedure maintains high particle solubility in aqueous solvent, which is a fundamental aspect to allow their applicability (as shown in Figure 1c). The crystal structure of the as-synthesized $CsPbX_3$ NCs inside the SiO_2 NSs and respective size distributions were studied via X-ray diffraction (XRD) and TEM, as reported in Figures 1d and S3, respectively. The XRD patterns show, in every case, a broad diffraction peak at 23° due to the contribution of amorphous SiO_2. The diffraction peaks of the $CsPbBr_3$−SiO_2 NSs at 21.36°, 26.32°, and 30.42° match cubic $CsPbBr_3$ structure. Consistent with their mixed halide composition, the XRD pattern of $CsPbBr_{1.5}I_{1.5}$−SiO_2 NSs shows the coexistence of cubic $CsPbBr_3$, the emissive γ-phase of $CsPbI_3$ (peaks at 20.09°, 28.48°, and 28.92°) together with traces of the optically passive orthorhombic $CsPbBr_{1.5}I_{1.5}$ δ-phase (peaks at 27.21°, 25.70°, and 31.31°); this is expected considering the thermodynamically favored crystalline transition of the $CsPbI_3$ γ-phase into the δ-phase below 150 °C.[74] Finally, the spectrum of $CsPbI_3$−SiO_2 NSs shows the γ-phase peaks and a more prominent contribution by the δ-phase. The emission properties of the $CsPbX_3$−SiO_2 NSs were studied using optical and X-ray excitation, and the corresponding PL and RL spectra are reported in Figure 1e. Consistent with previous results, both the PL and RL spectra progressively shift from the green to the NIR spectral regions with increasing iodine content.[21] In all three samples, the PL spectra show the narrow peak due to excitonic emission, indicating the absence of side products or emitting defect states introduced by the confined growth in the SiO_2 NS templates. The PL quantum efficiency was found to be 55 ± 5%, 21 ± 4%, and 12 ± 3% for $CsPbBr_3$, $CsPbBr_{1.5}I_{1.5}$, and $CsPbI_3$, respectively.

The PL decay time of all NSs reported in Figure S4 is consistent with previous reports and features a dominant radiative fast component followed by a minor contribution due to delayed fluorescence by back-transfer from shallow traps.[35] The RL spectra are slightly red-shifted compared to the respective PL, which possibly originates from the radiative recombination of shallow emissive defect states in the proximity of energy bands typically due to halide surface vacancies as already observed in colloidal $CsPbBr_3$ NCs.[35,75]

Next, we proceeded with validating the potential of $CsPbX_3$−SiO_2 NSs as X-ray sensitizer by studying the production of the singlet oxygen ($^1O_2$) species in aqueous environment under X-ray irradiation. In these experiments, schematically depicted in Figure 2a, we dispersed identical concentrations of $CsPbX_3$−SiO_2 NSs (2 mg/mL) with different halide composition in a phosphate buffer solution (PBS) to artificially mimic the physiological pH conditions; the same experiment was performed with bare SiO_2 NS as reference. The commercially available fluorescent probe singlet oxygen sensor green (SOSG) was used to monitor *in situ* the $^1O_2$ evolution. In its unoxidized form, SOSG is nonemissive, whereas its endoperoxide derivative formed upon oxidation by $^1O_2$ exhibits a characteristic PL band at 530 nm (Figure S5). Therefore, the SOSG PL intensity can be used to quantify the $^1O_2$ concentration during X-ray irradiation. The PL spectra of SOSG excited at 473 nm with a cw laser in PBS solutions of $CsPbX_3$−SiO_2 NSs were collected during 10 min of continuous exposure to soft X-rays (E_{max} = 20 keV) with 0.5 Gy/s dose rate. The X-ray excitation of $CsPbX_3$−SiO_2 NSs simultaneously triggers the sensitization of $^1O_2$ production and the NSs RL. In fact, the ability to emit RL while simultaneous sensitizing ROS production represents an important feature of our systems with respect to common radio-activated photosensitizers such as porphyrin-based assemblies that produce $^1O_2$ via energy transfer to the triplet states of molecular O_2 at the expense of their luminescence. Such a feature, combined with preserving their RL emission after significant amount of radiation (as shown in Figure 2b), offers the possibility of using $CsPbX_3$−SiO_2 NSs also as efficient radio-stimulated bio markers for *in vitro* or *in vivo* radio-imaging.

In Figure 2c we report the integrated intensity of the SOSG PL during the scan for the $CsPbX_3$−SiO_2 NSs as well as for the control solution containing bare SiO_2 NS; on the right axis we report the respective $^1O_2$ concentrations as extracted via the calibration procedure described in the Supporting Information. Notably, all solutions containing $CsPbX_3$−SiO_2 NSs exhibit systematically higher $^1O_2$ production with respect to bare SiO_2 NSs, with a 3-fold, 10-fold, and 13-fold enhancement along the series $CsPbBr_3$−SiO_2, $CsPbBr_{1.5}I_{1.5}$−SiO_2, and $CsPbI_3$−SiO_2 NSs, which indicates the substantial effect of the $CsPbX_3$ NCs on the $^1O_2$ generation.

Importantly, as shown in Figure 2d for the $CsPbI_3$−SiO_2 NSs (the other samples are reported in Figure S7), when the X-ray irradiation was momentarily interrupted and the solution was excited solely by the 473 nm laser, no additional $^1O_2$ was created, and the trend proceeded identically only after the X-irradiation was reestablished. This is relevant since the PL of $CsPbI_3$−SiO_2 NSs at 685 nm (1.81 eV) excited by the 473 nm laser source is partially resonant to the triplet state of O_2 (1.62 eV[77]) and could, in principle, produce $^1O_2$ via nonradiative energy transfer, similar to what occurs with common radio-activated photosensitizers.[78,79] The absence of $^1O_2$ production without X-rays therefore indicates that the process is a direct result of the interaction of ionizing radiation with the $CsPbI_3$−SiO_2 NSs with negligible mediation by its excitonic states; we note that the absence of ET despite the energy resonance could be due to the relatively large distance between the NCs and the particle surfaces imposed by the calcination procedure, as well as by the relatively fast decay time of the NC PL (4−8 ns) with respect to the micro-to-millisecond PL of sensitizer phosphorescence.[79,80] Consistent with the $^1O_2$ production being dominated by the interaction probability between the $CsPbX_3$−SiO_2 NSs and the X-rays, we found remarkably good correlation between the $^1O_2$ production rate and the halide composition. Specifically, as shown in Figure 2e, in which we report the $^1O_2$ production rate extracted from the linear fitting of the curves in Figure 2c, the NSs containing iodine-based NCs, namely $CsPbBr_{1.5}I_{1.5}$−SiO_2 and $CsPbI_3$−SiO_2, exhibited a substantially higher $^1O_2$ generation rate compared to the $CsPbBr_3$−SiO_2. This trend correlates well with the mass attenuation coefficient of the systems reported in Figure 2f (calculated using the NIST database[76] and EDX analysis reported in Figure S8) in the energy range of the soft X-rays used in our experiments, which is a direct consequence of their halide composition (with the other constituents being identical). As expected based on the higher Z of I with respect to Br (53 vs 35), the mass attenuation coefficient of the NCs monotonically grows with increasing iodine content, which results in increasing release of energy in the surrounding environment and subsequently larger $^1O_2$ generation rate. In fact, in the case of X-rays, the primary interactions occur by

https://doi.org/10.1021/acsenergylett.3c00234
ACS Energy Lett. 2023, 8, 1795−1802

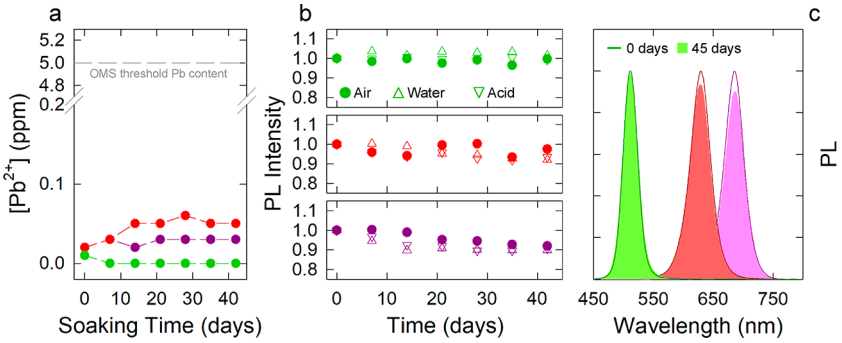

Figure 3. (a) Residual concentration of Pb^{2+} in 2 mg/mL solution of $CsPbBr_3$−MSN (green plot), $CsPbBr_{1.5}I_{1.5}$−MSN (red plot), and $CsPbI_3$−MSN (violet plot) in water as a function of soaking time. The concentrations were measured through inductively coupled plasma−optical emission spectrometry (ICP-OES). (b) PL intensity of $CsPbBr_3$−MSN (green markers), $CsPbBr_{1.5}I_{1.5}$−MSN (red markers), and $CsPbI_3$−MSN (violet markers) as a function of time in different storage conditions: in air (filled circles), in water solution (triangles up), in strong acid solution (HCl 1M, triangles down). PL emission was excited with a 405 nm laser. (c) Representative PL spectra of $CsPbBr_3$−MSN (green plot), $CsPbBr_{1.5}I_{1.5}$−MSN (red plot), and $CsPbI_3$−MSN (violet plot) at different soaking time in acid solution (pH 1) showing no modification of emission profile.

photoelectric effect or by inelastic Compton scattering, resulting in an avalanche of highly energetic secondary carriers that release their energy while traveling through a medium resulting in its ionization/excitation. Since the free path of secondary carriers is typically longer than the NS size, a substantial fraction of energy effectively escapes from the nanoparticle and is released for long distances along the ionization track, leading, in our case, to the observed strong sensitization of $^1O_2$ production.[19]

Notably, recent studies[81,82] demonstrated that a significant fraction of energy is deposited within the nanoparticles despite the primary interaction being shared between the nanoparticles themselves and the surrounding aqueous media. Indeed, energetic secondary charges exhibit migration ranges in most cases larger than the small nanoparticle size; consequently, a fraction of energy escapes from the nanoparticle and is released for long distances along the ionization track, directly activating the ROS production in water and the direct DNA cell damage.

Based on the promising $^1O_2$ sensitization rate of $CsPbI_3$−SiO_2 NSs, we further assessed their radiation resistance after 60 Gy, corresponding to the total dose that an RT patient cumulates in the entire RT treatment, as reported in Figure S9, in which the RL spectra collected before and after irradiation show that $CsPbI_3$−SiO_2 retained more than 80% of its initial RL emission intensity.

Finally, to further corroborate the potential suitability of $CsPbX_3$−SiO_2 NSs for X-ray stimulated applications, we assessed the risk related to the potential contamination of the environment by leakage of Pb atoms.

For this purpose, we monitored the concentration of Pb^{2+} in a water solution containing $CsPbX_3$−SiO_2 NSs (0.5 mg/mL) for 42 days by means of inductively coupled plasma−optical emission spectrometry (ICP-OES). The results, reported in Figure 3a, highlight that the concentration of Pb^{2+} was close to the sensitivity of ICP-OES, which settles a detection limit of 10 μg/L for the Pb^{2+} concentration. Considering the initial concentration of our $CsPbX_3$−SiO_2 NSs, we estimate that the amount of released Pb^{2+} in the monitored period is well below the 5 μg/g threshold established by the World Health Organization. To offer an illustrative comparison, if we consider a radiotherapy treatment involving the use of 10 mg of $CsPbX_3$−SiO_2 for a period of time comparable to our test, the total amount of lead introduced into the body would be equal to that which would be obtained by consuming 250 g of white rice.

Finally, we monitored the optical properties of our $CsPbX_3$−SiO_2 NSs in ambient atmosphere (55% humidity), water, and acid solution (1 M HCl, pH 1) in order to assess their long-time stability in conditions of potential biological interest. As shown in Figure 3b,c, nearly identical trends are observed in any condition, with nearly complete retention of the PL intensity for the $CsPbBr_3$−SiO_2 and $CsPbBr_{1.5}I_{1.5}$−SiO_2 NSs and a slight (ca. 10%) loss for the $CsPbI_3$−SiO_2 NSs, and the spectral properties are perfectly retained by all systems (complete spectra are reported in Figure S10).

In summary, we synthesized and studied ultrastable $CsPbX_3$−SiO_2 NSs combining the strong interaction probability and scintillation features of lead halide NCs with the robustness of silica. We demonstrated that such $CsPbX_3$−SiO_2 NSs dramatically sensitize the production of $^1O_2$ in water under X-ray stimulation and that the generation rate correlates well with their halide composition that leads to marked differences in their mass attenuation coefficient. Our data further indicate that the $^1O_2$ production is a direct result of the release of highly energetic secondary carriers in the environment and does not require quenching of their radioluminescence, thus potentially enabling their use as both therapeutic agents and radio-markers. Finally, we proved that our NSs retain their optical properties in aqueous and harsh pH conditions and under prolonged exposure to ionizing radiation. These results offer guidelines for the design of high-Z radio-sensitizers for enhancing the localized therapeutic effect of RT, reducing the delivered dose and consequent damage toward healthy tissues and thus potentially improving the quality of life of patients during and after radiological treatments.

■ ASSOCIATED CONTENT

Supporting Information

The Supporting Information is available free of charge at https://pubs.acs.org/doi/10.1021/acsenergylett.3c00234.

Detailed description of the NS synthesis and experimental methods; characterization data such as MSN and NC size distribution, time-resolved PL, temperature, and stability of PL spectra in acidic and basic solutions (PDF)

https://doi.org/10.1021/acsenergylett.3c00234
ACS Energy Lett. 2023, 8, 1795−1802

AUTHOR INFORMATION

Corresponding Authors

Francesco Carulli − *Università degli Studi di Milano-Bicocca, Dipartimento di Scienza dei Materiali, 20125 Milan, Italy;* orcid.org/0000-0002-8345-6606; Email: francesco.carulli@unimib.it

Liang Li − *Macao Institute of Materials Science and Engineering (MIMSE), Macau University of Science and Technology, Taipa 999078 Macao, China;* orcid.org/0000-0003-3898-0641; Email: lli@must.edu.mo

Sergio Brovelli − *Università degli Studi di Milano-Bicocca, Dipartimento di Scienza dei Materiali, 20125 Milan, Italy;* orcid.org/0000-0002-5993-855X; Email: sergio.brovelli@unimib.it

Authors

Mengda He − *School of Environmental Science and Engineering, Shanghai Jiao Tong University, Shanghai 200240, China;* orcid.org/0000-0002-1971-8034

Francesca Cova − *Università degli Studi di Milano-Bicocca, Dipartimento di Scienza dei Materiali, 20125 Milan, Italy;* orcid.org/0000-0001-7367-109X

Andrea Erroi − *Università degli Studi di Milano-Bicocca, Dipartimento di Scienza dei Materiali, 20125 Milan, Italy*

Complete contact information is available at: https://pubs.acs.org/10.1021/acsenergylett.3c00234

Author Contributions

†F. Carulli, M. He, and F. Cova contributed equally to this work

Notes

The authors declare no competing financial interest.

ACKNOWLEDGMENTS

This work received funding from the European Union's Horizon 2020 Research and Innovation programme under grant agreement no. 101004761 (AIDAINNOVA). This work was supported by Joint Funds of the National Natural Science Foundation of China (No. U21A20320), the National Natural Science Foundation of China (NSFC 22175113), "Pioneer" and "Leading Goose" R&D Program of Zhejiang (2022C03002), and the Start-up Founding for Scientific Research from Macau University of Science and Technology (SSF-22-001-MIMSE). We gratefully acknowledge Prof. Anna Vedda for her valuable help.

REFERENCES

(1) Zhang, L.; Gu, F.; Chan, J.; Wang, A.; Langer, R.; Farokhzad, O. Nanoparticles in Medicine: Therapeutic Applications and Developments. *Clinical Pharmacology & Therapeutics* **2008**, *83* (5), 761−769.

(2) Crapanzano, R.; Secchi, V.; Villa, I. Co-Adjuvant Nanoparticles for Radiotherapy Treatments of Oncological Diseases. *Applied Sciences* **2021**, *11* (15), 7073.

(3) Gao, X.; Cui, Y.; Levenson, R. M.; Chung, L. W. K.; Nie, S. In vivo cancer targeting and imaging with semiconductor quantum dots. *Nat. Biotechnol.* **2004**, *22* (8), 969−976.

(4) Li, L.; Wang, W.; Tang, J.; Wang, Y.; Liu, J.; Huang, L.; Wang, Y.; Guo, F.; Wang, J.; Shen, W.; Belfiore, L. A. Classification, Synthesis, and Application of Luminescent Silica Nanoparticles: a Review. *Nanoscale Res. Lett.* **2019**, *14* (1), 190.

(5) Liu, M.; Johnston, M. B.; Snaith, H. J. Efficient planar heterojunction perovskite solar cells by vapour deposition. *Nature* **2013**, *501* (7467), 395.

(6) Dong, H.; Du, S.-R.; Zheng, X.-Y.; Lyu, G.-M.; Sun, L.-D.; Li, L.-D.; Zhang, P.-Z.; Zhang, C.; Yan, C.-H. Lanthanide Nanoparticles: From Design toward Bioimaging and Therapy. *Chem. Rev.* **2015**, *115* (19), 10725−10815.

(7) Zarschler, K.; Rocks, L.; Licciardello, N.; Boselli, L.; Polo, E.; Garcia, K. P.; De Cola, L.; Stephan, H.; Dawson, K. A. Ultrasmall inorganic nanoparticles: State-of-the-art and perspectives for biomedical applications. *Nanomedicine: Nanotechnology, Biology and Medicine* **2016**, *12* (6), 1663−1701.

(8) Li, M.; Luo, Z.; Zhao, Y. Self-Assembled Hybrid Nanostructures: Versatile Multifunctional Nanoplatforms for Cancer Diagnosis and Therapy. *Chem. Mater.* **2018**, *30* (1), 25−53.

(9) Jaque, D.; Martínez Maestro, L.; del Rosal, B.; Haro-Gonzalez, P.; Benayas, A.; Plaza, J. L.; Martín Rodríguez, E.; García Solé, J. Nanoparticles for photothermal therapies. *Nanoscale* **2014**, *6* (16), 9494−9530.

(10) Lucky, S. S.; Soo, K. C.; Zhang, Y. Nanoparticles in Photodynamic Therapy. *Chem. Rev.* **2015**, *115* (4), 1990−2042.

(11) Wong, X. Y.; Sena-Torralba, A.; Álvarez-Diduk, R.; Muthoosamy, K.; Merkoçi, A. Nanomaterials for Nanotheranostics: Tuning Their Properties According to Disease Needs. *ACS Nano* **2020**, *14* (3), 2585−2627.

(12) Jin, J.; Zhao, Q. Engineering nanoparticles to reprogram radiotherapy and immunotherapy: recent advances and future challenges. *J. Nanobiotechnol.* **2020**, *18* (1), 75.

(13) Pratt, E. C.; Shaffer, T. M.; Grimm, J. Nanoparticles and radiotracers: advances toward radionanomedicine. *WIREs Nanomedicine and Nanobiotechnology* **2016**, *8* (6), 872−890.

(14) Chen, H. H. W.; Tien Kuo, M. Improving radiotherapy in cancer treatment: Promises and challenges. *Oncotarget* **2017**, *8* (37), 62742−62758.

(15) Haume, K.; Rosa, S.; Grellet, S.; Śmiałek, M. A.; Butterworth, K. T.; Solov'yov, A. V.; Prise, K. M.; Golding, J.; Mason, N. J. Gold nanoparticles for cancer radiotherapy: a review. *Cancer Nanotechnology* **2016**, *7* (1), 8.

(16) Azzam, E. I.; Jay-Gerin, J.-P.; Pain, D. Ionizing radiation-induced metabolic oxidative stress and prolonged cell injury. *Cancer Letters* **2012**, *327* (1), 48−60.

(17) Ling, C. C.; Humm, J.; Larson, S.; Amols, H.; Fuks, Z.; Leibel, S.; Koutcher, J. A. Towards multidimensional radiotherapy (MD-CRT): biological imaging and biological conformality. *International Journal of Radiation Oncology Biology Physics* **2000**, *47* (3), 551−560.

(18) Clement, S.; Campbell, J. M.; Deng, W.; Guller, A.; Nisar, S.; Liu, G.; Wilson, B. C.; Goldys, E. M. Mechanisms for Tuning Engineered Nanomaterials to Enhance Radiation Therapy of Cancer. *Advanced Science* **2020**, *7* (24), 2003584.

(19) Klein, J. S.; Sun, C.; Pratx, G. Radioluminescence in biomedicine: physics, applications, and models. *Physics in Medicine & Biology* **2019**, *64* (4), 04TR01.

(20) Dey, A.; Ye, J.; De, A.; Debroye, E.; Ha, S. K.; Bladt, E.; Kshirsagar, A. S.; Wang, Z.; Yin, J.; Wang, Y.; Quan, L. N.; Yan, F.; Gao, M.; Li, X.; Shamsi, J.; Debnath, T.; Cao, M.; Scheel, M. A.; Kumar, S.; Steele, J. A.; Gerhard, M.; Chouhan, L.; Xu, K.; Wu, X.-g.; Li, Y.; Zhang, Y.; Dutta, A.; Han, C.; Vincon, I.; Rogach, A. L.; Nag, A.; Samanta, A.; Korgel, B. A.; Shih, C.-J.; Gamelin, D. R.; Son, D. H.; Zeng, H.; Zhong, H.; Sun, H.; Demir, H. V.; Scheblykin, I. G.; Mora-Seró, I.; Stolarczyk, J. K.; Zhang, J. Z.; Feldmann, J.; Hofkens, J.; Luther, J. M.; Pérez-Prieto, J.; Li, L.; Manna, L.; Bodnarchuk, M. I.; Kovalenko, M. V.; Roeffaers, M. B. J.; Pradhan, N.; Mohammed, O. F.; Bakr, O. M.; Yang, P.; Müller-Buschbaum, P.; Kamat, P. V.; Bao, Q.; Zhang, Q.; Krahne, R.; Galian, R. E.; Stranks, S. D.; Bals, S.; Biju, V.; Tisdale, W. A.; Yan, Y.; Hoye, R. L. Z.; Polavarapu, L. State of the Art and Prospects for Halide Perovskite Nanocrystals. *ACS Nano* **2021**, *15* (7), 10775−10981.

(21) Protesescu, L.; Yakunin, S.; Bodnarchuk, M. I.; Krieg, F.; Caputo, R.; Hendon, C. H.; Yang, R. X.; Walsh, A.; Kovalenko, M. V. Nanocrystals of Cesium Lead Halide Perovskites (CsPbX3, X = Cl, Br, and I): Novel Optoelectronic Materials Showing Bright Emission with Wide Color Gamut. *Nano Lett.* **2015**, *15* (6), 3692−3696.

(22) Cao, M.; Xu, Y.; Li, P.; Zhong, Q.; Yang, D.; Zhang, Q. Recent advances and perspectives on light emitting diodes fabricated from halide metal perovskite nanocrystals. *Journal of Materials Chemistry C* **2019**, *7* (46), 14412−14440.
(23) Brown, A. A. M.; Damodaran, B.; Jiang, L.; Tey, J. N.; Pu, S. H.; Mathews, N.; Mhaisalkar, S. G. Lead Halide Perovskite Nanocrystals: Room Temperature Syntheses toward Commercial Viability. *Adv. Energy Mater.* **2020**, *10* (34), 2001349.
(24) Shamsi, J.; Urban, A. S.; Imran, M.; De Trizio, L.; Manna, L. Metal Halide Perovskite Nanocrystals: Synthesis, Post-Synthesis Modifications, and Their Optical Properties. *Chem. Rev.* **2019**, *119* (5), 3296−3348.
(25) Liu, M.; Wan, Q.; Wang, H.; Carulli, F.; Sun, X.; Zheng, W.; Kong, L.; Zhang, Q.; Zhang, C.; Zhang, Q.; Brovelli, S.; Li, L. Suppression of temperature quenching in perovskite nanocrystals for efficient and thermally stable light-emitting diodes. *Nat. Photonics* **2021**, *15* (5), 379−385.
(26) Jana, A.; Cho, S.; Patil, S. A.; Meena, A.; Jo, Y.; Sree, V. G.; Park, Y.; Kim, H.; Im, H.; Taylor, R. A. Perovskite: Scintillators, direct detectors, and X-ray imagers. *Mater. Today* **2022**, *55*, 110−136.
(27) Zhou, F.; Li, Z.; Lan, W.; Wang, Q.; Ding, L.; Jin, Z. Halide Perovskite, a Potential Scintillator for X-Ray Detection. *Small Methods* **2020**, *4* (10), 2000506.
(28) Heo, J. H.; Shin, D. H.; Park, J. K.; Kim, D. H.; Lee, S. J.; Im, S. H. High-Performance Next-Generation Perovskite Nanocrystal Scintillator for Nondestructive X-Ray Imaging. *Adv. Mater.* **2018**, *30* (40), 1801743.
(29) Zhou, J.; An, K.; He, P.; Yang, J.; Zhou, C.; Luo, Y.; Kang, W.; Hu, W.; Feng, P.; Zhou, M.; Tang, X. Solution-Processed Lead-Free Perovskite Nanocrystal Scintillators for High-Resolution X-Ray CT Imaging. *Advanced Optical Materials* **2021**, *9* (11), 2002144.
(30) Wang, B.; Li, P.; Zhou, Y.; Deng, Z.; Ouyang, X.; Xu, Q. $Cs_3Cu_2I_5$ Perovskite Nanoparticles in Polymer Matrix as Large-Area Scintillation Screen for High-Definition X-ray Imaging. *ACS Applied Nano Materials* **2022**, *5* (7), 9792−9798.
(31) Liu, Y.; Zaffalon, M. L.; Zito, J.; Cova, F.; Moro, F.; Fanciulli, M.; Zhu, D.; Toso, S.; Xia, Z.; Infante, I.; De Trizio, L.; Brovelli, S.; Manna, L. Cu+ → Mn2+ Energy Transfer in Cu, Mn Coalloyed Cs3ZnCl5 Colloidal Nanocrystals. *Chem. Mater.* **2022**, *34* (19), 8603−8612.
(32) Liu, F.; Wu, R.; Wei, J.; Nie, W.; Mohite, A. D.; Brovelli, S.; Manna, L.; Li, H. Recent Progress in Halide Perovskite Radiation Detectors for Gamma-Ray Spectroscopy. *ACS Energy Letters* **2022**, *7* (3), 1066−1085.
(33) Knoll, G. F. *Radiation Detection and Measurement*; John Wiley & Sons, 2010; pp 29−64.
(34) Zhu, D.; Zaffalon, M. L.; Zito, J.; Cova, F.; Meinardi, F.; De Trizio, L.; Infante, I.; Brovelli, S.; Manna, L. Sb-Doped Metal Halide Nanocrystals: A 0D versus 3D Comparison. *ACS Energy Letters* **2021**, *6* (6), 2283−2292.
(35) Zaffalon, M. L.; Cova, F.; Liu, M.; Cemmi, A.; Di Sarcina, I.; Rossi, F.; Carulli, F.; Erroi, A.; Rodà, C.; Perego, J.; Comotti, A.; Fasoli, M.; Meinardi, F.; Li, L.; Vedda, A.; Brovelli, S. Extreme γ-ray radiation hardness and high scintillation yield in perovskite nanocrystals. *Nat. Photonics* **2022**, *16* (12), 860−868.
(36) Gandini, M.; Villa, I.; Beretta, M.; Gotti, C.; Imran, M.; Carulli, F.; Fantuzzi, E.; Sassi, M.; Zaffalon, M.; Brofferio, C.; Manna, L.; Beverina, L.; Vedda, A.; Fasoli, M.; Gironi, L.; Brovelli, S. Efficient, fast and reabsorption-free perovskite nanocrystal-based sensitized plastic scintillators. *Nat. Nanotechnol.* **2020**, *15* (6), 462−468.
(37) Rakhymzhan, A.; Leben, R.; Zimmermann, H.; Günther, R.; Mex, P.; Reismann, D.; Ulbricht, C.; Acs, A.; Brandt, A. U.; Lindquist, R. L.; Winkler, T. H.; Hauser, A. E.; Niesner, R. A. Synergistic Strategy for Multicolor Two-photon Microscopy: Application to the Analysis of Germinal Center Reactions In Vivo. *Sci. Rep.* **2017**, *7* (1), 7101.
(38) Yuan, L.; Lin, W.; Zhao, S.; Gao, W.; Chen, B.; He, L.; Zhu, S. A Unique Approach to Development of Near-Infrared Fluorescent Sensors for in Vivo Imaging. *J. Am. Chem. Soc.* **2012**, *134* (32), 13510−13523.
(39) López-Valverde, J. A.; Jiménez-Ortega, E.; Leal, A. Clinical Feasibility Study of Gold Nanoparticles as Theragnostic Agents for Precision Radiotherapy. *Biomedicines* **2022**, *10* (5), 1214.
(40) Talianov, P. M.; Peltek, O. O.; Masharin, M.; Khubezhov, S.; Baranov, M. A.; Drabavičius, A.; Timin, A. S.; Zelenkov, L. E.; Pushkarev, A. P.; Makarov, S. V.; Zyuzin, M. V. Halide Perovskite Nanocrystals with Enhanced Water Stability for Upconversion Imaging in a Living Cell. *J. Phys. Chem. Lett.* **2021**, *12* (37), 8991−8998.
(41) Zhang, H.; Wang, X.; Liao, Q.; Xu, Z.; Li, H.; Zheng, L.; Fu, H. Embedding Perovskite Nanocrystals into a Polymer Matrix for Tunable Luminescence Probes in Cell Imaging. *Adv. Funct. Mater.* **2017**, *27* (7), 1604382.
(42) Zhao, P.; Jiang, Y.; Tang, Z.; Li, Y.; Sun, B.; Wu, Y.; Wu, J.; Liu, Y.; Bu, W. Constructing Electron Levers in Perovskite Nanocrystals to Regulate the Local Electron Density for Intensive Chemodynamic Therapy. *Angew. Chem., Int. Ed.* **2021**, *60* (16), 8905−8912.
(43) Grisorio, R.; Di Clemente, M. E.; Fanizza, E.; Allegretta, I.; Altamura, D.; Striccoli, M.; Terzano, R.; Giannini, C.; Irimia-Vladu, M.; Suranna, G. P. Exploring the surface chemistry of cesium lead halide perovskite nanocrystals. *Nanoscale* **2019**, *11* (3), 986−999.
(44) Huang, H.; Bodnarchuk, M. I.; Kershaw, S. V.; Kovalenko, M. V.; Rogach, A. L. Lead Halide Perovskite Nanocrystals in the Research Spotlight: Stability and Defect Tolerance. *ACS Energy Letters* **2017**, *2* (9), 2071−2083.
(45) Yuan, S.; Chen, D.; Li, X.; Zhong, J.; Xu, X. In Situ Crystallization Synthesis of CsPbBr3 Perovskite Quantum Dot-Embedded Glasses with Improved Stability for Solid-State Lighting and Random Upconverted Lasing. *ACS Appl. Mater. Interfaces* **2018**, *10* (22), 18918−18926.
(46) Huang, H.; Chen, B.; Wang, Z.; Hung, T. F.; Susha, A. S.; Zhong, H.; Rogach, A. L. Water resistant CsPbX3 nanocrystals coated with polyhedral oligomeric silsesquioxane and their use as solid state luminophores in all-perovskite white light-emitting devices. *Chemical Science* **2016**, *7* (9), 5699−5703.
(47) Wei, Y.; Deng, X.; Xie, Z.; Cai, X.; Liang, S.; Ma, P. a.; Hou, Z.; Cheng, Z.; Lin, J. Enhancing the Stability of Perovskite Quantum Dots by Encapsulation in Crosslinked Polystyrene Beads via a Swelling−Shrinking Strategy toward Superior Water Resistance. *Adv. Funct. Mater.* **2017**, *27* (39), 1703535.
(48) Wang, S.; Huang, W.; Liu, X.; Wang, S.; Ye, H.; Yu, S.; Song, X.; Liu, Z.; Wang, P.; Yang, T.; Chu, D.; Gou, J.; Yuan, M.; Chen, L.; Su, B.; Liu, S.; Zhao, K. Ruddlesden−Popper Perovskite Nanocrystals Stabilized in Mesoporous Silica with Efficient Carrier Dynamics for Flexible X-Ray Scintillator. *Adv. Funct. Mater.* **2023**, *33*, 2210765.
(49) Chen, P.; Liu, Y.; Zhang, Z.; Sun, Y.; Hou, J.; Zhao, G.; Zou, J.; Fang, Y.; Xu, J.; Dai, N. In situ growth of ultrasmall cesium lead bromine quantum dots in a mesoporous silica matrix and their application in flexible light-emitting diodes. *Nanoscale* **2019**, *11* (35), 16499−16507.
(50) Park, S.; An, M. N.; Almeida, G.; Palazon, F.; Spirito, D.; Krahne, R.; Dang, Z.; De Trizio, L.; Manna, L. CsPbX3/SiOx (X = Cl, Br, I) monoliths prepared via a novel sol−gel route starting from Cs4PbX6 nanocrystals. *Nanoscale* **2019**, *11* (40), 18739−18745.
(51) Konidakis, I.; Brintakis, K.; Kostopoulou, A.; Demeridou, I.; Kavatzikidou, P.; Stratakis, E. Highly luminescent and ultrastable cesium lead bromide perovskite patterns generated in phosphate glass matrices. *Nanoscale* **2020**, *12* (25), 13697−13707.
(52) Dirin, D. N.; Benin, B. M.; Yakunin, S.; Krumeich, F.; Raino, G.; Frison, R.; Kovalenko, M. V. Microcarrier-Assisted Inorganic Shelling of Lead Halide Perovskite Nanocrystals. *ACS Nano* **2019**, *13* (10), 11642−11652.
(53) Pan, A.; Wu, Y.; Yan, K.; Yu, Y.; Jurow, M. J.; Ren, B.; Zhang, C.; Ding, S.; He, L.; Liu, Y. Stable Luminous Nanocomposites of Confined Mn2+-Doped Lead Halide Perovskite Nanocrystals in Mesoporous Silica Nanospheres as Orange Fluorophores. *Inorg. Chem.* **2019**, *58* (6), 3950−3958.

(54) He, M.; Zhang, Q.; Carulli, F.; Erroi, A.; Wei, W.; Kong, L.; Yuan, C.; Wan, Q.; Liu, M.; Liao, X.; Zhan, W.; Han, L.; Guo, X.; Brovelli, S.; Li, L. Ultra-stable, Solution-Processable CsPbBr3-SiO2 Nanospheres for Highly Efficient Color Conversion in Micro Light-Emitting Diodes. *ACS Energy Letters* **2023**, *8* (1), 151−158.
(55) Zhang, Q. G.; Wang, B.; Zheng, W. L.; Kong, L.; Wan, Q.; Zhang, C. Y.; Li, Z. C.; Cao, X. Y.; Liu, M. M.; Li, L. Ceramic-like stable CsPbBr3 nanocrystals encapsulated in silica derived from molecular sieve templates. *Nat. Commun.* **2020**, *11*, 31.
(56) Zhang, Q.; Sun, X.; Zheng, W.; Wan, Q.; Liu, M.; Liao, X.; Hagio, T.; Ichino, R.; Kong, L.; Wang, H.; Li, L. Band Gap Engineering toward Wavelength Tunable CsPbBr3 Nanocrystals for Achieving Rec. 2020 Displays. *Chem. Mater.* **2021**, *33* (10), 3575−3584.
(57) Zhang, Q.; Zheng, W.; Wan, Q.; Liu, M.; Feng, X.; Kong, L.; Li, L. Confined Synthesis of Stable and Uniform CsPbBr 3 Nanocrystals with High Quantum Yield up to 90% by High Temperature Solid-State Reaction. *Advanced Optical Materials* **2021**, *9*, 2002130.
(58) Zhang, Q.; He, M.; Wan, Q.; Zheng, W.; Liu, M.; Zhang, C.; Liao, X.; Zhan, W.; Kong, L.; Guo, X.; Li, L. Suppressing thermal quenching of lead halide perovskite nanocrystals by constructing a wide-bandgap surface layer for achieving thermally stable white light-emitting diodes. *Chemical Science* **2022**, *13* (13), 3719−3727.
(59) Lin, Y.; Fan, X.; Yang, X.; Zheng, X.; Huang, W.; Shangguan, Z.; Wang, Y.; Kuo, H. C.; Wu, T.; Chen, Z. Remarkable Black-Phase Robustness of CsPbI 3 Nanocrystals Sealed in Solid SiO 2 /AlO x Sub-Micron Particles. *Small* **2021**, *17*, 2103510.
(60) Wang, H.-C.; Lin, S.-Y.; Tang, A.-C.; Singh, B. P.; Tong, H.-C.; Chen, C.-Y.; Lee, Y.-C.; Tsai, T.-L.; Liu, R.-S. Mesoporous Silica Particles Integrated with All-Inorganic CsPbBr3 Perovskite Quantum-Dot Nanocomposites (MP-PQDs) with High Stability and Wide Color Gamut Used for Backlight Display. *Angew. Chem., Int. Ed.* **2016**, *55* (28), 7924−7929.
(61) Liu, Z.; Sinatra, L.; Lutfullin, M.; Ivanov, Y. P.; Divitini, G.; De Trizio, L.; Manna, L. One Hundred-Nanometer-Sized CsPbBr3/m-SiO2 Composites Prepared via Molten-Salts Synthesis are Optimal Green Phosphors for LCD Display Devices. *Adv. Energy Mater.* **2022**, *12* (38), 2201948.
(62) Ravi, V. K.; Scheidt, R. A.; Nag, A.; Kuno, M.; Kamat, P. V. To Exchange or Not to Exchange. Suppressing Anion Exchange in Cesium Lead Halide Perovskites with PbSO4−Oleate Capping. *ACS Energy Letters* **2018**, *3* (4), 1049−1055.
(63) Ravi, V. K.; Saikia, S.; Yadav, S.; Nawale, V. V.; Nag, A. CsPbBr3/ZnS Core/Shell Type Nanocrystals for Enhancing Luminescence Lifetime and Water Stability. *ACS Energy Letters* **2020**, *5* (6), 1794−1796.
(64) Nie, W.; Tsai, H. Perovskite nanocrystals stabilized in metal−organic frameworks for light emission devices. *Journal of Materials Chemistry A* **2022**, *10* (37), 19518−19533.
(65) Hou, J.; Chen, P.; Shukla, A.; Krajnc, A.; Wang, T.; Li, X.; Doasa, R.; Tizei, L. H. G.; Chan, B.; Johnstone, D. N.; Lin, R.; Schülli, T. U.; Martens, I.; Appadoo, D.; Ari, M. S.; Wang, Z.; Wei, T.; Lo, S.-C.; Lu, M.; Li, S.; Namdas, E. B.; Mali, G.; Cheetham, A. K.; Collins, S. M.; Chen, V.; Wang, L.; Bennett, T. D. Liquid-phase sintering of lead halide perovskites and metal-organic framework glasses. *Science* **2021**, *374* (6567), 621−625.
(66) Sun, K.; Tan, D.; Fang, X.; Xia, X.; Lin, D.; Song, J.; Lin, Y.; Liu, Z.; Gu, M.; Yue, Y.; Qiu, J. Three-dimensional direct lithography of stable perovskite nanocrystals in glass. *Science* **2022**, *375* (6578), 307−310.
(67) Wang, B.; Zhang, C.; Zheng, W.; Zhang, Q.; Bao, Z.; Kong, L.; Li, L. Large-Scale Synthesis of Highly Luminescent Perovskite Nanocrystals by Template-Assisted Solid-State Reaction at 800 °C. *Chem. Mater.* **2020**, *32* (1), 308−314.
(68) Lin, J.; Lu, Y.; Li, X.; Huang, F.; Yang, C.; Liu, M.; Jiang, N.; Chen, D. Perovskite Quantum Dots Glasses Based Backlit Displays. *ACS Energy Letters* **2021**, *6* (2), 519−528.
(69) Tsai, H.; Shrestha, S.; Vilá, R. A.; Huang, W.; Liu, C.; Hou, C.-H.; Huang, H.-H.; Wen, X.; Li, M.; Wiederrecht, G.; Cui, Y.; Cotlet, M.; Zhang, X.; Ma, X.; Nie, W. Bright and stable light-emitting diodes made with perovskite nanocrystals stabilized in metal−organic frameworks. *Nat. Photonics* **2021**, *15* (11), 843−849.
(70) Malgras, V.; Tominaka, S.; Ryan, J. W.; Henzie, J.; Takei, T.; Ohara, K.; Yamauchi, Y. Observation of Quantum Confinement in Monodisperse Methylammonium Lead Halide Perovskite Nanocrystals Embedded in Mesoporous Silica. *J. Am. Chem. Soc.* **2016**, *138* (42), 13874−13881.
(71) Qian, C.-X.; Deng, Z.-Y.; Yang, K.; Feng, J.; Wang, M.-Z.; Yang, Z.; Liu, S.; Feng, H.-J. Interface engineering of CsPbBr3/TiO2 heterostructure with enhanced optoelectronic properties for all-inorganic perovskite solar cells. *Appl. Phys. Lett.* **2018**, *112* (9), 093901.
(72) Ding, N.; Zhou, D.; Sun, X.; Xu, W.; Xu, H.; Pan, G.; Li, D.; Zhang, S.; Dong, B.; Song, H. Highly stable and water-soluble monodisperse CsPbX3/SiO2 nanocomposites for white-LED and cells imaging. *Nanotechnology* **2018**, *29* (34), 345703.
(73) Dirin, D. N.; Protesescu, L.; Trummer, D.; Kochetygov, I. V.; Yakunin, S.; Krumeich, F.; Stadie, N. P.; Kovalenko, M. V. Harnessing Defect-Tolerance at the Nanoscale: Highly Luminescent Lead Halide Perovskite Nanocrystals in Mesoporous Silica Matrixes. *Nano Lett.* **2016**, *16* (9), 5866−5874.
(74) Cui, J.; Liu, Y.; Deng, Y.; Lin, C.; Fang, Z.; Xiang, C.; Bai, P.; Du, K.; Zuo, X.; Wen, K.; Gong, S.; He, H.; Ye, Z.; Gao, Y.; Tian, H.; Zhao, B.; Wang, J.; Jin, Y. Efficient light-emitting diodes based on oriented perovskite nanoplatelets. *Science Advances* **2021**, *7* (41), No. eabg8458.
(75) Rodà, C.; Fasoli, M.; Zaffalon, M. L.; Cova, F.; Pinchetti, V.; Shamsi, J.; Abdelhady, A. L.; Imran, M.; Meinardi, F.; Manna, L.; Vedda, A.; Brovelli, S. Understanding Thermal and A-Thermal Trapping Processes in Lead Halide Perovskites Towards Effective Radiation Detection Schemes. *Adv. Funct. Mater.* **2021**, *31* (43), 2104879.
(76) Hubbell, J. H.; Seltzer, S. M. *NIST Standard Reference Database 126*, May 1996 ed.; National Insititute of Standards and Technology, 1996.
(77) Schweitzer, C.; Schmidt, R. Physical Mechanisms of Generation and Deactivation of Singlet Oxygen. *Chem. Rev.* **2003**, *103* (5), 1685−1758.
(78) Tavakkoli Yaraki, M.; Liu, B.; Tan, Y. N. Emerging Strategies in Enhancing Singlet Oxygen Generation of Nano-Photosensitizers Toward Advanced Phototherapy. *Nano-Micro Letters* **2022**, *14* (1), 123.
(79) Schweitzer, C.; Mehrdad, Z.; Noll, A.; Grabner, E.-W.; Schmidt, R. Mechanism of Photosensitized Generation of Singlet Oxygen during Oxygen Quenching of Triplet States and the General Dependence of the Rate Constants and Efficiencies of O2(1Σg+), O2(1Δg), and O2(3Σg-) Formation on Sensitizer Triplet State Energy and Oxidation Potential. *J. Phys. Chem. A* **2003**, *107* (13), 2192−2198.
(80) DeRosa, M. C.; Crutchley, R. J. Photosensitized singlet oxygen and its applications. *Coord. Chem. Rev.* **2002**, *233*−*234*, 351−371.
(81) Bulin, A.-L.; Vasil'ev, A.; Belsky, A.; Amans, D.; Ledoux, G.; Dujardin, C. Modelling energy deposition in nanoscintillators to predict the efficiency of the X-ray-induced photodynamic effect. *Nanoscale* **2015**, *7*, 5744−5751.
(82) Belsky, A.; Ivanovskikh, K.; Vasil'ev, A.; Joubert, M.-F.; Dujardin, C. Estimation of the Electron Thermalization Length in Ionic Materials. *J. Phys. Chem. Lett.* **2013**, *4*, 3534−3538.

https://doi.org/10.1021/acsenergylett.3c00234
ACS Energy Lett. 2023, 8, 1795−1802